

Ag₂Cu₃Cr₂O₈(OH)₄: A new bidimensional silver-copper mixed -oxyhydroxide with in-plane ferromagnetic coupling

Nieves Casañ-Pastor¹, Jordi Rius¹, Oriol Vallcorba², Inma Peral², Judith Oró-Solé¹, Daniel S. Cook³, Richard I. Walton³, Alberto García¹, David Muñoz-Rojas⁴

1 Institut de Ciència de Materials de Barcelona, CSIC, Campus UAB, Bellaterra 08193, Spain

2 Alba synchrotron, 08290 Cerdanyola del Valles, Barcelona, Spain

3 Department of Chemistry, University of Warwick, Coventry, CV4 7AL, UK

4 LMGP, University Grenoble-Alpes, CNRS, F-38016 Grenoble, France

Ag₂Cu₃Cr₂O₈(OH)₄, a new Ag-Cu-Cr-O layered mixed oxide prepared by soft hydrothermal heterogeneous reactions is reported. The new phase is an oxohydroxide and presents a structure with alternating brucite-like Cu-O and Ag-O layers and connected by individual chromate groups. The crystallographic structure has been solved and refined from high resolution powder X-ray diffraction data and is supported by density functional theory calculations yielding a triclinic, space group $P\bar{1}$, $a = 5.3329(1)$ Å, $b = 5.3871(1)$ Å, $c = 10.0735(1)$ Å, $\alpha = 80.476(1)^\circ$, $\beta = 87.020(1)^\circ$, $\gamma = 62.383(1)^\circ$. Bond valence sums suggest the formulation Ag+2Cu₂+3Cr+2O₈(OH)₄, an electronic state fully supported by X-ray photoelectron spectroscopy (XPS) and Cr K-edge X-ray absorption near edge structure (XANES) measurements. Ag₂Cu₃Cr₂O₈(OH)₄ exhibits bidimensional Cu-O-Cu ferromagnetic correlations that are apparent at much higher temperatures than in other similar Cu-O layered structures, without coupling between Cu-O layers which represents a unique case in the recent family of silver copper oxides. The role of Ag inducing bidimensionality in copper oxides is therefore expanded further with the presence of chromate anions. Ab initio calculations using density function theory show that the electronic states involved originate mainly from Cu and OH orbitals, with minor contributions from Cr and the O atoms linking the Cr tetrahedra to the brucitic Cu-O layer, and almost no contribution from Ag. Further modeling of the in-plane magnetic interactions between Cu atoms suggests that coupled magnetized stripes are responsible for the observed behavior. The results are discussed in relation with previous Ag-Cu mixed oxide phases where metallic behavior or ferro-antiferro transitions had been observed. The structure of this new Ag-Cu-O phase as compared with previous silver copper oxides supports the conclusion that Ag-Cu layered ordering is favored in oxidizing conditions.

1. Introduction

In the search of new bidimensional mixed copper oxides, silver has been a surprise yielding new layered Ag-Cu-O phases with significant potential in terms of electronic properties and structures, and possible implications in fields such as high temperature superconductivity,^{1,2} multiferroics,³ energy storage,⁴ all-oxide solar cells,⁵⁻⁷ microelectronic devices,^{8,9} or transparent electronics.^{10,11} Previously, copper oxide phases had shown great interest in cases such as Cu₂O combined with ZnO for ultra-low cost solar cells,¹²⁻¹⁵ p-type transparent Cu-based oxides such as CuAlO₂ or Cu₂O,^{10,16-18} as well as high T_c superconductors,^{1,2} and their applications had been expanded further by doping. With an initial objective focus on designing layered copper oxides resembling those high T_c superconductors, in particular Ag joining Cu-O layers instead of other toxic elements as mercury,¹⁹ our group developed the first silver copper mixed oxide.^{20,21} Surprisingly, no binary Ag-Cu-O phases are known to exist in nature, despite the

existence of mixed sulfides or phosphates and other complex oxychloride phases.²² Although it was considered that silver would impose the need of high pressure conditions to be part of the copper oxide, the soft chemistry reactions described below show otherwise and have yielding us to a rich chemistry and phases with relevant properties. This first silver-copper oxide, $\text{Ag}_2\text{Cu}_2\text{O}_3$, was obtained by an acid base slow process, and presents a three-dimensional structure resembling that of natural mineral paramelaconite $\text{Cu}_2\text{Cu}_2\text{O}_3$, containing Cu^+ and Cu^{+2} ions.²⁰ In a oxygen-doping attempt, electrochemical direct solid state oxidation of $\text{Ag}_2\text{Cu}_2\text{O}_3$ at room temperature yielded $\text{Ag}_2\text{Cu}_2\text{O}_4$ (also named AgCuO_2),²³⁻²⁵ a phase with an additional oxygen atom per Cu that could also be prepared from single silver and copper salts or metals, and by oxidation with ozone²⁶ or persulfate²⁷ ions. Significantly, $\text{Ag}_2\text{Cu}_2\text{O}_4$ crystallizes in a 2D crednerite structure with alternating Ag and Cu layers, and possesses a peculiar electronic structure in which Ag and Cu present intermediate oxidation states ($\text{Ag}^{(1+\square)^+}$, $\text{Cu}^{(2+\square)^+}$) and presents charge delocalization between all the elements, including oxygen atoms, as shown by X-ray photoelectron spectroscopy (XPS) and X-ray absorption spectroscopy (XAS) experiments.²⁵ Accordingly, $\text{Ag}_2\text{Cu}_2\text{O}_4$ presents unusually high conductivity^{28,29} and Pauli paramagnetism, although not superconductivity. It is remarkable that a solid state transformation occurs at room temperature and in alkaline aqueous media and involving the change from a 3D to a 2D structure. Oxygen intercalation had been observed before in layered copper oxides, as La_2CuO_4 intercalates up to 0.14 O atoms per Cu,^{29,30} also a room temperature process in which it becomes superconducting. However, the extent of oxygen intercalation in $\text{Ag}_2\text{Cu}_2\text{O}_3$, (one oxygen intercalated per Cu atom and up to 1.3 in the case of using ozone), the solid state process itself, and the ion mobility suspected, suggest that new possible phases may be formed depending on the oxidizing conditions using soft chemistry processes and very low temperatures. In fact, synthesis based on soft hydrothermal treatments at very low temperatures have shown significant changes in morphology and also have yielded new phases, a fact that supports the previous assumption.^{28,29}

Other oxidations reactions have been explored in our lab aiming to understand the chemistry and the possible new properties and solid state transformations at low temperatures in this Ag-Cu family. Thus, oxidation of Ag and Cu precursors in presence of KMnO_4 has yielded $\text{Ag}_2\text{CuMnO}_4$ in very soft hydrothermal conditions,³¹ with Ag and Cu also ordered in a 2D arrangement, and crystallizing in a 2D delafossite structure with Ag in the A layers and Cu and Mn in the B layers. In this example the oxidizing agent gets incorporated into the structure, while persulfate does not. The oxide is a p-type semiconductor, has Ag+1 and Cu+2 oxidation states and it presents much lower conductivity than AgCuO_2 since no charge delocalization occurs. But it shows ferromagnetic coupling within the Cu-Mn-O layers (with M-O-M angles near 90°) and antiferromagnetic coupling at lower temperature among layers. The role of Ag^+ d^{10} ions connecting the layers is thus relevant within the structure, since it induces antiferromagnetic coupling. Those pioneering works have awakened the interest in the wide range of Ag-Cu-O structures and electronic properties, possible multi-centered mixed valence species and bidimensional arrangements in the Ag-Cu family. Other new members have been reported,³²⁻³⁴ including phases such as high temperature high pressure perovskite $\text{AgCu}_3\text{V}_4\text{O}_{12}$ ³² which has mixed valence states. In all cases, the new Ag-Cu mixed oxides³⁵ have found significant value in catalysis, energy storage or transparent electronics.^{36,37} The electronic structure of this family has also received interest from a predictive theoretical point of view with recent publications of *ab initio* studies on the possibility of other Ag, Cu, and Au ternary oxides.³⁸

This work shows an alternative set of oxidizing conditions that yield a new bidimensional phase Ag-Cu-Cr mixed oxide with formula $\text{Ag}_2\text{Cu}_3\text{Cr}_2\text{O}_8(\text{OH})_4$, again with significant magnetic properties. Ferromagnetic coupling is observed between copper ions in the Cu-O layers, but, as opposed to $\text{Ag}_2\text{CuMnO}_4$, layers are

isolated magnetically from each other. The new compound has been obtained by a low temperature hydrothermal reaction in oxidizing conditions that contain dichromate but require larger temperature than the previous phases and the usual oxidized silver precursor, AgO, to prevent formation of metallic silver. The resulting electronic states are the usual Ag⁺, Cu⁺² and Cr⁺⁶. The structure has been solved by Patterson function direct methods from powder X-ray diffraction data. X-ray absorption near edge structure (XANES) at the Cr K-edge and XPS results confirm the metal oxidation states deduced from structure refinement, and electronic structure calculations support structure resolution and explain the interactions in the structure and within the bidimensional Cu-O layers.

2. Experimental

2.1 Synthesis. In a typical synthesis, 0.13 g of AgO (Aldrich), 0.39 g of CuSO₄·5H₂O (Fluka p.a.) and 0.09 g of K₂Cr₂O₇ (Sigma Aldrich ACS reagent 99%) were mixed in 12 ml of distilled water and stirred vigorously. Subsequently, 0.20 g of solid KOH were added to the suspension and it was stirred for 1 minute. The suspension was then transferred to a 23 ml TeflonTM-lined stainless steel Parr autoclave and introduced in an oven at 120 °C for 10 h. After natural cooling, the resulting precipitate was filtered, washed with water and dried at 50 °C. The same phase could also be obtained using 0.096 g of CrO₃ (instead of dichromate) and 0.125 g of NaOH. The new phase has been obtained by low temperature hydrothermal reaction, similar to our previous reports for other Ag-Cu-O phases.^{28,31} As for the preceding silver-copper oxides, AgO was chosen as Ag precursor to prevent reduction to metallic silver. The oxidant K₂Cr₂O₇ is not enough in these hydrothermal conditions to prevent silver reduction unless AgO is used. Although AgCuO₂ may be prepared from Ag⁺ precursors,²⁵ AgO has been proven to result optimal in non electrochemical conditions, as in the synthesis of Ag₂CuMnO₄, preventing the formation of metallic silver during the reaction.³¹ When using suspensions of solid precursors, such as AgO, the reaction kinetics are affected as well as the phases obtained and their morphologies (as it is the case for the reaction of solid Ag₂O with pyrrole monomers to yield tortuous hybrid nanostructures),⁵¹ but in the case of silver, although the mechanism of such heterogeneous solid-state redox reactions is not fully understood, the use of AgO has proved to be a versatile reagent for preparation of Ag oxides with different oxidation states for Ag. Although the phase has been obtained in pure form using Na₂Cr₂O₇ in excess as chromium precursor (with KOH as mineralizer typically used in hydrothermal reactions⁵²), it can also be obtained using CrO₃ as chromium precursor and NaOH as mineralizer.

2.2 Characterization. Powder X-ray diffraction (XRD) patterns were collected using a rotating anode Rigaku Rotaflex Ru-200B diffractometer with CuK α radiation ($\lambda_1 = 1.5406 \text{ \AA}$ and $\lambda_2 = 1.5444 \text{ \AA}$) with a step size of 0.02° and using a scanning rate of 0.16°/min. Scanning electron microscopy (SEM) images were obtained using a Philips XL-30 field-emission gun (FEG) and a JEOL JSM 6300. Energy dispersive analyses (EDX) analyses were performed but were not used for stoichiometry analyses since oxygen contents were showing that redox changes were seen to occur under the electron beam in that case. Magnetic properties were measured in a Quantum Design SQUID magnetometer, using a gelatin capsule to hold the well packed solid, with the centre of gravity of holder and sample coinciding. Zero field and field cooled measurements were compared for possible superconducting properties. Final susceptibility data was measured from 5 K to 300 K at 5000 Oe. Additionally, hysteresis curves were measured from 0 to 50000 Oe, at 5 K and 200 K. XPS measurements were performed at room temperature using a PHI 5500 Multitechnique System (from Physical Electronics) with a monochromatic X-Ray source (Aluminum K α : 1486.6 eV and 350 W) placed perpendicular to the analyzer axis. The analyzed area was a circle of 0.8 mm in diameter, and the selected resolution for the spectra was 187.5 eV of Pass Energy with 0.8 eV/step for

the general spectra, and 11.75 eV of Pass Energy and 0.05 eV/step for the high resolution spectra. XANES data were measured in transmission mode on beamline B18 at the Diamond Light Source (UK) at the Cr K-edge.³⁹ Pellets were prepared by grinding ~20 mg of the oxide samples into ~80 mg of polyethylene powder before being pressed into 13 mm diameter pellets of thickness ~1 mm. Data were also recorded from the crystalline reference materials Cr₂O₃, CrO₃ and Na₂Cr₂O₇ and simultaneous measurement of a chromium foil was used to provide calibration. Normalization of the data was performed by subtracting linear pre-edge and polynomial post-edge backgrounds using the software Athena.⁴⁰

2.3 Synchrotron Powder X-ray data collection and determination. Synchrotron data of the samples in a capillary were acquired with two different set-ups: i) for indexing, the sample was illuminated with a microfocused beam and the corresponding 2D diffraction pattern was collected on a flat CCD detector ($\lambda=0.4243$ Å); ii) for crystal structure solution and Rietveld refinement, data were obtained by focusing the beam onto a 1D Mythen-II microstrip detector ($\lambda= 0.70558$ Å determined from peak positions of a NIST Si standard) to reduce peak broadening caused by the capillary. All experiments were performed at beamline 4 at ALBA synchrotron.⁴¹ Indexing was carried out using TREOR90.⁴² The model-free profile refinement was made using Dajust,⁴³ using Mythen-II data. The crystal structure was solved in **P1** by applying cluster-based Patterson-function direct methods (Xlens_PD6).⁴⁴ The number of reflections was 253 for a resolution limit fixed at $d_{\min}=1.28$ Å, which represented 63 refined phases. The default number of phase-refinement trials was 50. The bond-valence method⁴⁵ was used to estimate the internal consistency of valences of both cations and oxygen in the refined structure.

2.4 Theoretical Simulations. Density functional Theory (DFT) and DFT+U ALBERTO? U ?calculations were used to complement the structural refinement process and to investigate the electronic structure effects leading to the ferromagnetic coupling within the Cu layers. We employed the SIESTA code,⁴⁶ which uses norm-conserving pseudopotentials and finite-range numerical-orbital basis sets. For the structure-related work we performed geometry optimizations starting from the preliminary diffraction refinement data, using a conjugate-gradient algorithm to minimize the forces on the atoms. For the analysis of the electronic structure we used the tools included in the SIESTA distribution to compute band structures and partial densities of states. We employed double-theta plus polarization basis sets optimized with a fictitious external pressure of 0.05 GPa.⁴⁷ The real-space mesh had a cutoff of 350 Ry and the k-point sampling was generated with an effective length cutoff of 16 Å,⁴⁸ both appropriately converged. We used a gradient-corrected PBE exchange and correlation functional,⁴⁹ and the DFT+U corrections were implemented following the scheme in Ref.⁵⁰ Monte Carlo simulations of a simple Ising model were used to explore magnetic interactions in the material, employing a simulation domain with 40 × 40 unit cells, each containing three sites in a hexagonal arrangement to represent the Cu atoms in the brucitic layers of the compound. The standard Metropolis algorithm was used, and susceptibility data obtained from the analysis of the magnetization fluctuations.

3. Results and Discussion

As for previous Ag-Cu oxides made by hydrothermal reactions, the Ag-Cu-Cr-O morphology obtained is greatly dependent on experimental parameters. This new phase, formulated as Ag₂Cu₃Cr₂O₈(OH)₄ from structure resolution described below, precipitates as an intense ruby-red powder made of micron size platelet-shaped crystals (See inset in Figure 1). The size of the final crystals, and their agglomeration, depends also on the reaction parameters, in particular reaction time, excess of dichromate used and reaction temperature yielding to preferential orientation. The resulting crystals are larger than those

obtained for previously reported AgCuO_2 or $\text{Ag}_2\text{CuMnO}_4$ (microns vs. nanometers, respectively),^{28,31} using similar reaction times.

Powder X-ray diffraction patterns of the new compound were obtained from samples prepared under different synthesis conditions (Figure 2(a)). Some variations of intensity due to some preferential orientation were observed depending on the microstructure. For that reason, the material used for the crystal structure determination was measured in a glass capillary ($\mu\text{R}= 2.95$) after being carefully ground in an agathe mortar to reduce preferential orientation (March coefficient is 1.07).

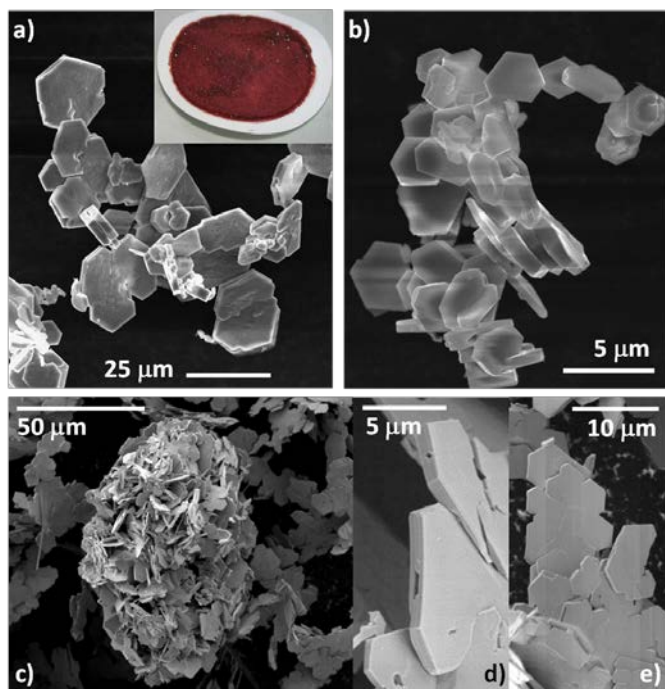


Figure 1. SEM images of $\text{Ag}_2\text{Cu}_3\text{Cr}_2\text{O}_8(\text{OH})_4$. A macroscopic view of $\text{Ag}_2\text{Cu}_3\text{Cr}_2\text{O}_8(\text{OH})_4$ powder is shown in the inset of (a).

The crystal structure of the new Ag-Cu-Cr-O mixed phase was solved by applying cluster-based Patterson-function direct methods in $P\bar{1}$ (see supplementary material for complete details).⁴⁴ The Fourier map of the trial with best Figure of Merit (FOM) showed most of the Cu and Ag atoms. The structure was completed by Fourier syntheses coupled to Rietveld refinements. Figure 2(b) shows the experimental and refined patterns while Table 1 summarizes relevant crystallographic data and refinement details. The positions of the H atoms were determined by DFT calculations (see below). Resulting atomic positions are included in the Supplementary Material.

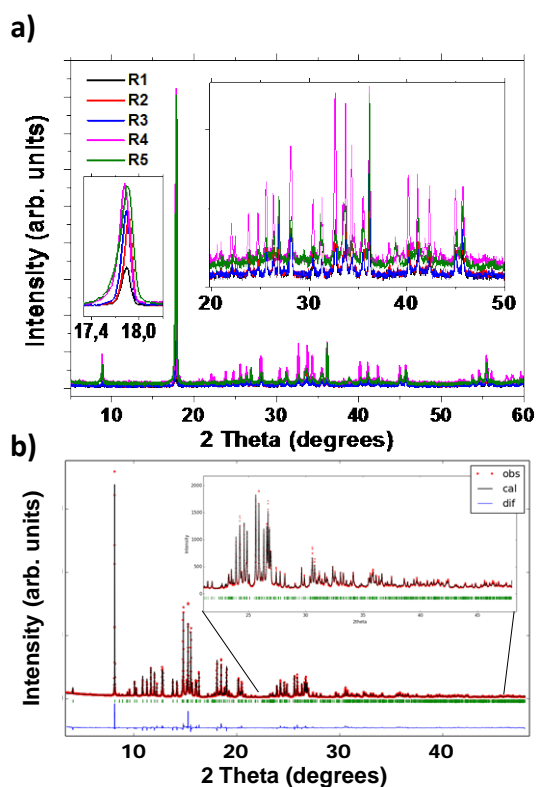


Figure 2. a) Raw XRD patterns of the powders obtained from several reactions where R1 represents the synthesis described here. Insets show expanded regions where differences in peak intensities for different products can be clearly seen. b) final profile fit from Rietveld refinement of the structure of the novel Ag-Cu mixed compound $\text{Ag}_2\text{Cu}_3\text{Cr}_2\text{O}_8(\text{OH})_4$.

Table 1. Crystallographic data for $\text{Ag}_2\text{Cu}_3\text{Cr}_2\text{O}_8(\text{OH})_4$.

| Chemical formula | $\text{Ag}_2\text{Cu}_3\text{Cr}_2\text{O}_8(\text{OH})_4$ |
|---------------------------------------|--|
| Crystal color | Ruby red |
| Crystal habit | Quasi-hexagonal plates |
| a (Å) | 5.3329(1) |
| b (Å) | 5.3871(1) |
| c (Å) | 10.0735(1) |
| α (°) | 80.476(1) |
| β (°) | 87.020(1) |
| γ (°) | 62.383(1) |
| Volume (Å ³) | 252.79(1) |
| Z | 1 |
| Formula weight (g mol ⁻¹) | 706.39 |
| Crystal System | Triclinic |
| Space group (No.) | $P\bar{1}$, (2) |
| Measurement Temperature (K) | 300 |

| | |
|--|---------|
| Wavelength (Å) | 0.70558 |
| Calculated density (g/cm ³) | 4.614 |
| R_p $\frac{\sum y_{i,obs} - y_{i,cal} }{\sum y_{i,obs}}$ | = 0.069 |
| R_F $\frac{\sum F_{obs} - F_{cal} }{\sum F_{obs} }$ | = 0.044 |
| R_B $\frac{\sum Y_{obs} - Y_{cal} }{\sum Y_{obs} }$ | = 0.092 |
| R_{wp} | 0.088 |
| $R_{wp} = \left[\frac{\sum w_i y_{i,obs} - y_{i,cal} ^2}{\sum w_i y_{i,obs}^2} \right]^{1/2}$ where $w_i = 1/\sigma_{i,cal}^2$ | |

The crystal structure of the title compound consists of two alternating layers: a brucite-like layer of composition $[\text{Cu}_3(\text{OH})_4\text{O}_2]^{2-}$, with one copper atom sitting on an inversion center, and a brucite-like layer of composition $[(\text{Ag}_{2,\square})\text{O}_6]^{10-}$ with vacancies in one third of the positions. Therefore a bidimensional arrangement of MO_6 edge-sharing octahedra ($M = \text{Cu}, \text{Ag}$ in each layer) occurs. Both layers are held together by two tetrahedral Cr^{6+}O_4 units (see Figure 3(a)). Although X-ray diffraction is not sensitive to H atoms, the presence of OH groups is required for charge balance and it is typical of brucite-like structures, together with the expected irregularities for the coordination polyhedra of Cu^{2+} (Jahn-Teller effect) and Ag^+ (possible trend to linearity), prompted us to use DFT calculations to elucidate the H positions and to support the refinements. O 1s XPS results confirm the existence of OH^- entities even from a semiquantitative point of view. (See Figure 4, and Supplementary Material S1) The octahedra in the Cu layer are distorted due to the Jahn-Teller effect associated with Cu^{2+} . In contrast, in the case of the Ag sheet, the Ag octahedra are remarkably regular, not usual for $\text{Ag}(I)$. For the initial restrained Rietveld refinement, the expected mean cation-O distance for each polyhedron was introduced. Starting from a set of preliminary-refinement atomic positions, we used the SIESTA code⁴⁶ to optimize the internal coordinates while maintaining the lattice vectors at their experimental values. The results were broadly compatible with the average bond-distances from initial refinement of the coordination polyhedra. The extra DFT coordinate information was fed back into a further refinement in the form of individual restraints, leading to the final structure (see refined atomic coordinates and distances in Tables S1 and S2). The introduction of the DFT restraints in the Rietveld refinement produced no residual increase [$R_{wp}=0.088$, $\chi=1.51$] and confirmed the occurrence of long Jahn-Teller Cu-O bonds, as well as the overall structure. Finally, bond valence analysis^{45,53} was performed (see Table 2) to check the internal chemical consistency of the refined model. Results are coherent and indicate the presence of Ag^+ , Cu^{2+} , Cr^{6+} and O^{2-} oxidation states.

Table S2 shows the M-O bond lengths of the structure. Figure 3(a) and (b) show a perspective view of the structure layered arrangement and the in-plane bond lengths and angles that are relevant for the electronic structure of the material.

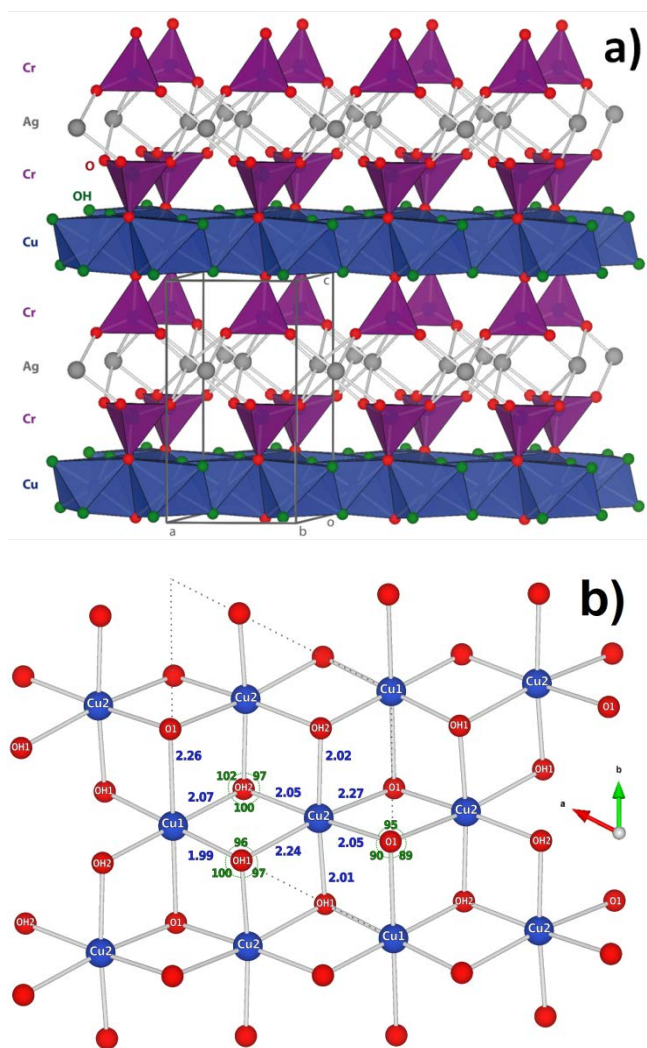


Figure 3. a) Perspective view of the crystal structure of the title compound showing the alternating Cu (blue) and Ag (grey) brucite-like layers held together by Cr⁶⁺ (purple). b) Upper view of the copper brucite-like layer showing the copper coordination polyhedra, where angles Cu-O-Cu have near 90° values. (Blue: Cu-O bond lengths in Å; green: Cu-O-Cu bond angles in °).

The new compound was studied by XPS in order to verify the oxidation states obtained from the refinement. XPS survey spectra of the powder showed all the elements present in the structure, with no other impurity being present (see Supplementary Information for the survey spectrum). Ag $3d$ peaks, at 374 and 368 eV, agree with those reported for Ag¹⁺, as in Ag₂Cu₂O₃ or Ag₂CuMnO₄, and as opposed to AgCuO₂ that shows a splitting of Ag peaks and a shift to lower binding energies due to the higher oxidation state of silver (regardless of the synthetic method used²⁸). In the case of copper, Cu $2p$ peaks at 935 and 955 eV are present. The obtained binding energies for Cu are slightly larger than for Ag₂Cu₂O₃ or Ag₂CuMnO₄, which present the Cu $2p$ peaks at 933 and 934.2 eV, respectively,^{24,31} but are still consistent with reported values for Cu²⁺.^{54–56} Also, the presence of the satellites at higher binding energy, which are absent for Cu³⁺,⁵⁷ supports the oxidation state of Cu²⁺ in Ag₂Cu₃Cr₂O₈(OH)₄. For Cr, the two obtained peaks at 579.2 and 588.5 eV correspond to Cr⁶⁺ ions.^{54,58} Finally, in the case of oxygen, the O $1s$ peak is quite broad and anisotropic, and can indeed be deconvoluted into two signals that would correspond to O²⁻ and

OH⁻, at 632.5 and 630.5 eV, respectively^{24,31} (see Figure 4). Deconvolution based on that hypothesis renders a OH⁻/O^{total} ratio ≈ 25%, and therefore, (taking into account the possible error in deconvolution), is in good agreement with the observed OH⁻/O^{total} ratio from the structure refinement (33%) and confirms the presence of OH⁻ groups in the proposed brucite-related structure.

Table 2. Bond valences (ν) for the title compound computed from individual cation–O distances (d in Å) with expression $\nu = \exp((R_{\text{cation}} - d)/0.37)$ where R_{cation} values are, respectively, 1.679, 1.805 and 1.794 for Cu²⁺, Ag⁺ and Cr⁶⁺.^{45,53} $\Sigma \nu_{\text{Cations}}$ gives the sum of valences from the cations bonded to the anion; likewise, $\Sigma \nu_{\text{O}}$ represents the sum of the contributions of the metals to O atoms. * The factor 2 is introduced to take into account the contributions to Cu1 of the O1, OH1 and OH2 related by the symmetry center.

| | Cu1 | Cu2 | Ag1 | Cr1 | $\Sigma \nu_{\text{O}}$ |
|-------------------------------|-------------------------|-------------|-------------|-------------|-------------------------|
| O1 | 0.21 | 0.20, 0.37 | | 1.15 | 1.93 |
| O2 | | | 0.17, 0.22 | 1.38 | 1.77 |
| O3 | | | 0.20, 0.17 | 1.36 | 1.73 |
| O4 | | | 0.19, 0.19 | 1.48 | 1.86 |
| OH1 | 0.43 | 0.41, 0.22 | | | 1.06 |
| OH2 | 0.35 | 0.37, 0.40 | | | 1.12 |
| $\Sigma \nu_{\text{Cations}}$ | 0.99 x 2* = 1.98 | 1.97 | 1.14 | 5.37 | |

The XPS Cr2p surface results were also confirmed by XANES Cr K-edge spectra, which indicate the presence of Cr⁶⁺. The strong pre-edge feature at ~5992 eV is the formally forbidden 1s-3d transition that is seen in the materials with tetrahedrally coordinated Cr, where a centre of symmetry is absent. A closer look at the pre-edge feature reveals that for Ag₂Cu₃Cr₂O₈(OH)₄ the peak maximum appears at slightly lower energy than for K₂Cr₂O₇ and CrO₃, and that it is slightly more intense (see Figure 5 inset). This is consistent with the presence of isolated chromate units, as opposed to dichromate dimmers or CrO₃-like polymeric chains, as shown by Farges who studied a variety of chromium oxide materials.⁵⁹ It can also be seen that the post-edge region of the XANES spectrum (beyond 6025 eV) of Ag₂Cu₃Cr₂O₈(OH)₄ is very different from that in K₂Cr₂O₇ and CrO₃, again in agreement with the refined structure, in which individual CrO₄²⁻ units, not condensed, link the brucite-like Cu and Ag layers.

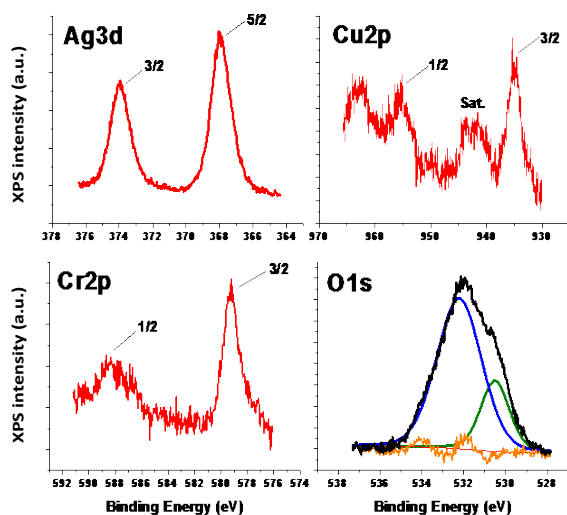


Figure 4. XPS spectra of $\text{Ag}_2\text{Cu}_3\text{Cr}_2\text{O}_8(\text{OH})_4$ for the Ag 3d, Cu 2p, Cr 2p and O 1s lines, (and satellites) and deconvolution for O 1s peaks (blue corresponding to O^{2-} and green corresponding to OH^-).

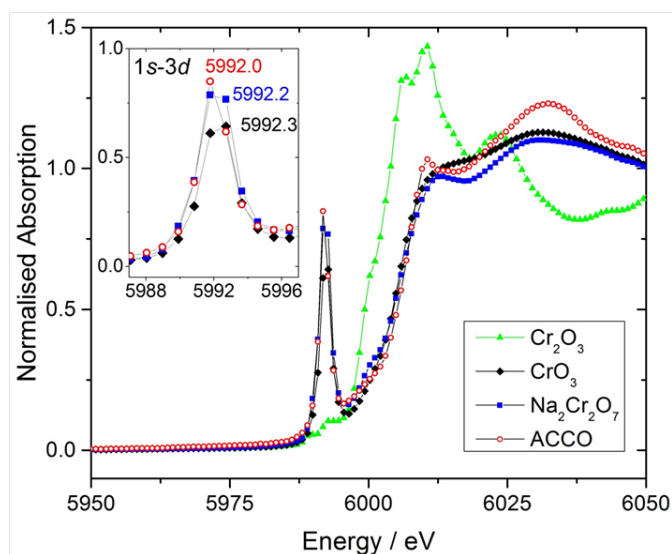


Figure 5. Cr K-edge XANES spectra for Cr_2O_3 , CrO_3 , $\text{Na}_2\text{Cr}_2\text{O}_7$ and $\text{Ag}_2\text{Cu}_3\text{Cr}_2\text{O}_8(\text{OH})_4$ (ACCO). The inset shows an expanded region of the pre-edge feature with the position of the 1s-3d transition as determined by peak fitting.

χ_{molar} and $1/\chi_{\text{molar}}$ vs. T curves (Supplementary material Figure S2) apparently do not show spontaneous ordering. However, magnetic susceptibility measurements for $\text{Ag}_2\text{Cu}_3\text{Cr}_2\text{O}_8(\text{OH})_4$ show room temperature values of μ_{eff} (defined as $\sqrt{8\chi_{\text{molar}}T}$) around $3.2 \mu_{\text{B}}$, (cgs units) slightly above spin-only values for three uncoupled Cu^{2+}

ions per unit formula, $3.0 \mu_B$ (Figure 6(a)). As the temperature is lowered the moment starts increasing significantly at 190 K. The large enhancement in μ_{eff} indicates the presence of ferromagnetic exchange associated to the compound structural features described above, with Cu-O-Cu angles near 90° . For those angles, and within a 10° range, the orbital near-orthogonality dampens the natural antiferromagnetic coupling (Goodenough-Kanamori rules).⁶⁰⁻⁶³ The observed μ_{eff} behavior in the range 100-300 K resembles that of previously published $\text{Ag}_2\text{CuMnO}_4$,³¹ also with layered M-O layers (M = Cu and Mn disordered) in which the angles are close to 90° .

$\text{Ag}_2\text{Cu}_3\text{Cr}_2\text{O}_8(\text{OH})_4$ magnetization curves obtained at low and high temperatures are shown in Figure 6(b). Magnetization values at 5 K are almost but not completely saturated at the maximum field used of 50000 Oe, reaching $0.8 \mu_B$ per Cu atom, a value close to the $1 \mu_B$ expected for complete saturation of spin-1/2 units. No hysteric behavior is seen, which would be consistent in principle with a very soft ferromagnetism or (super) paramagnetism. It is worth remarking that other traditional ways of expressing χ_{molar} and $1/\chi_{\text{molar}}$ vs. T curves (Supplementary material Figure S2) are not sensitive to show the described behavior when similar with ferromagnetic couplings usually found in molecular cluster systems without long range order.⁶⁴

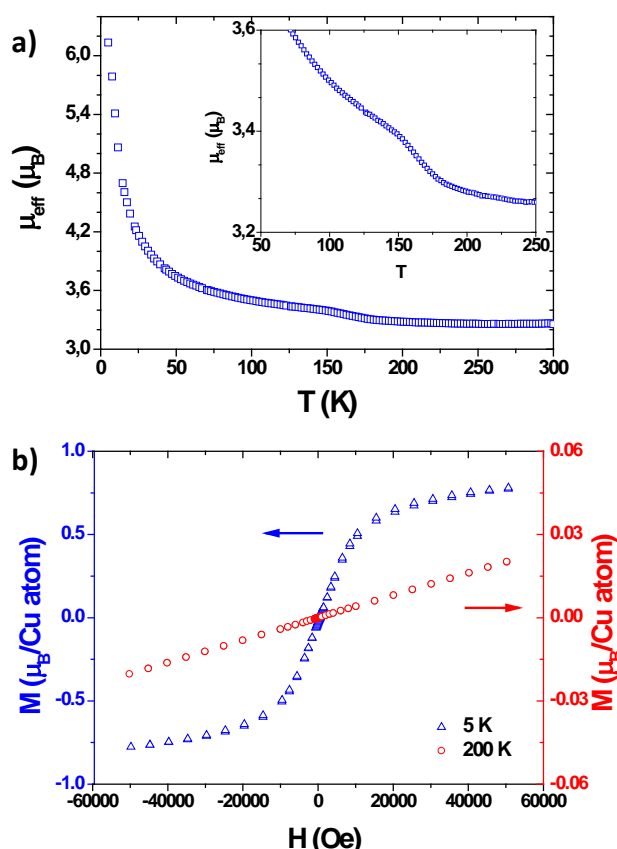


Figure 6. a) Effective magnetic moment defined as $\sqrt{8 \chi_{\text{molar}} T}$ versus T (K), expanded in the inset near the start of its enhancement. b) Magnetization (μ_B per Cu atom) Hysteresis curves (0-5 Tesla) at 5 K (blue) and at 200 K (red). See also Figure S2 in supplementary material for χ_{molar} and $1/\chi_{\text{molar}}$ behavior.

Two dimensional ferromagnetic coupling in copper oxides is not common but it has been described in other cases where Cu-O-Cu bond angles are near 90°, as in this case.^{65,66} and some minerals with brucite copper have long range order.⁶⁷ However, for layered hydroxo copper species with this type of structure the increase in μ_{eff} in those cases is apparent only below 25-40 K.^{65,66} It is very significant, therefore, the high temperature at which clear ferromagnetic interactions are observed in this phase. To the best of our knowledge, this example is unique in terms of the ferromagnetic correlation found in the Cu-O plane, even with no long range order and no hysteresis.

Theoretical modeling of magnetic behavior: To better understand the magnetic properties of this compound we have carried out spin-polarized electronic-structure calculations within DFT and DFT+U, using the SIESTA code. As described above, the three non equivalent Cu atoms (blue, green, and yellow in Figure S3 and 7 for Cu1, Cu2, and Cu3, respectively) sit at the center of edge-shared distorted oxygen octahedra. Some of the oxygen atoms belong to OH groups, while the rest are part of Cr-centered tetrahedra. The octahedra for Cu2 and Cu3 have an edge with linking oxygens in two CrO₄ groups, whereas in the case of Cu1 the CrO₄ groups are at opposite extremes of the octahedron. (See also Figure S4). The chromate groups can be considered as running in lines parallel to the b lattice vector.

These geometrical considerations are relevant to picture the pattern of magnetic interactions in the Cu layer. Edge-sharing of the octahedra implies that there are, in principle, two superexchange bridges for every Cu-Cu interaction. Neglecting minor differences in bond lengths and angles, bridges come in two broad kinds, depending on whether the oxygen atom involved belongs to an OH or a CrO₄ group. With the aim of simulating the essential features we have semi-quantitatively modeled the magnetic interactions within a Cu layer with an effective Hamiltonian with three parameters, corresponding to three classes of double bridges: *J*₁, both Cu-Cu paths including an O in a OH group; *J*₂: one path through OH and another through an O in a Cr group; *J*₃, both paths using O atoms in Cr groups. The model represents the energy of different spin configurations by a simple Ising model:

$$E = - \sum_{\langle ij \rangle} J_{ij} s_i s_j \quad (\text{Equation 1})$$

where s_i and s_j are +1 or -1 for spin up or down on the Cu atoms, and the sum is over pairs of nearest neighbors *i* and *j*. We are neglecting minor variations in Cu-Cu distances and Cu-O-Cu angles within a given double-bridge class in this approximate model (which otherwise would need nine coupling parameters). The pattern of interactions can be seen on Figure 7.

To estimate the values of *J*₁, *J*₂, and *J*₃, we prepared the system in different spin configurations for the three non equivalent Cu atoms and iterated the DFT self-consistency cycle until convergence in the charge densities (majority and minority) was achieved. In all cases the initial spin pattern was maintained.

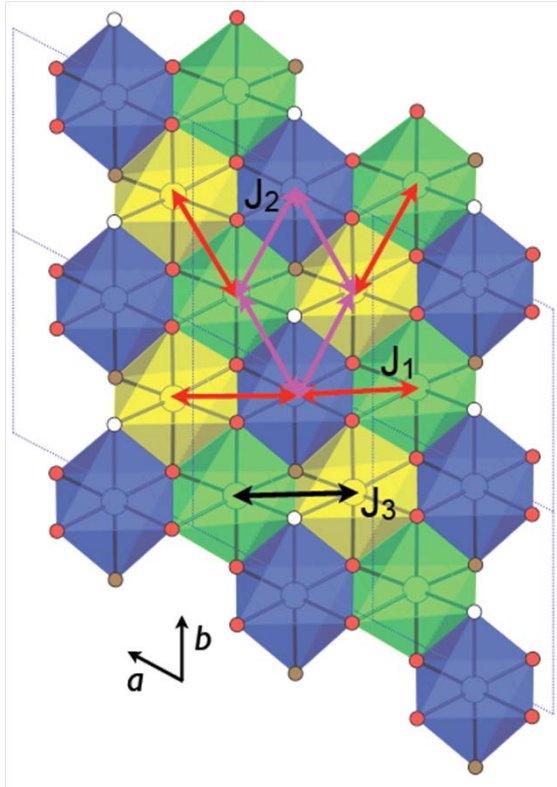


Figure 7. Pattern of exchange interactions for Cu in the brucitic layer, represented by arrows (J1: red, J2: purple, J3: black). Oxygen atoms belonging to OH groups are depicted in red. Those associated to chromate groups are colored in brown (upper side of the layer) and white (lower side of the layer).

To take into account the correlation effects for the Cu d electrons not appropriately accounted for in standard DFT, we also carried out calculations within the DFT+U approximation. The appropriate value of the effective Hubbard repulsion parameter U is not straightforward to determine. Here we have used a maximum value $U = 6$ eV, roughly estimated from the results of Himmetoglu et al for distorted forms of CuO ,⁶⁸ and performed calculations also at $U = 3$ eV to provide an intermediate reference.

The spin configurations that can be generated in the unit cell are: (***uuu***) with three “up” spins, ***duu***, in which the spin on Cu1 is opposite to those in Cu2 and Cu3, and ***udu*** and ***uud***, in which the spins of Cu2 and Cu3 are opposite to each other. The latter two are very close in energy, as expected from the structural features, and consistently with their equivalence in our model. Therefore, only three non equivalent spin configurations, are possible within the primitive unit cell providing just two energy differences. In order to have enough data to determine the three parameters of our model we doubled the cell along the a lattice vector to generate other configurations. In this extended cell we chose, apart from the reference fully polarized one ***uuu|uuu***, two zero-spin configurations, in which the spins in one half of the enlarged cell are opposite to those in the other half: ***uuu|ddd*** and ***duu|udd***.

Table 3. Energies of the different spin configurations. Up (u) and down (d) patterns correspond to the spin orientations of the Cu atoms, in the unit cell or in a doubled cell along a . The energies are relative to the completely polarized “up” configuration, and are given in meV per cell.

| U | ΔE | ΔE | ΔE | ΔE | J_1 | J_2 | J_3 |
|------|------------|------------|------------|------------|-------------|-------|-------|
| (eV) | (duu) | (udu) | (uuu/ddd) | (duu/udd) | | | |
| 0 | 49.3 | 8.0 | 16.8 | 98.5 | 1.0 | 5.66 | -10.3 |
| 3 | 22.1 | 2.2 | 0.7 | 44.1 | ≈ 0 | 2.76 | -4.42 |
| 6 | 11.5 | 2.4 | 1.3 | 22.9 | 0.1 | 1.40 | -1.84 |

Table 3 gives the energies of the spin configurations considered with respect to the fully polarized ones (**uuu** and **uuu|uuu**, respectively). As all the entries are positive, the configurations with complete alignment of spins are the lowest in energy, and the predicted ground state is thus ferromagnetic, although some of the energy differences are quite small, and in general they tend to decrease with increasing U . Before discussing the magnetic ordering features implied by these results, it is instructive to present an analysis of the electronic structure of the compound, starting with the case of $U=0$. The net ground-state spin of $3 \mu_B$ corresponds to the three unoccupied minority bands (in green) around -4.5 eV just above the gap in Figure 8(a).

Analysis of the partial density of states (see Figure 8(b)) indicates that those bands originate mainly from the Cu atoms and from the O atoms bonded to H, with minor contributions from Cr and from the O atoms linking the Cr tetrahedra to the brucitic Cu layer. These hole electronic states have therefore a clear two-dimensional character, being essentially confined to the brucitic Cu layers and the neighboring chromate groups.

With the introduction of the on-site repulsion U the Cu-derived empty bands are pushed up, thus increasing the band gap. The density of states plot in the inset of Figure 8(b), computed for $U=6$ eV, shows that these bands now overlap in energy with another set, associated mainly with the Cr groups. The rest of the electronic structure is basically unchanged. For example, the valence band edge moves only slightly due to the downward movement of the Cu-derived full bands. Analysis of the orbital populations shows that the net magnetization is still associated mainly to the Cu atoms and to the oxygens in OH groups, as shown above for the $U=0$ case.

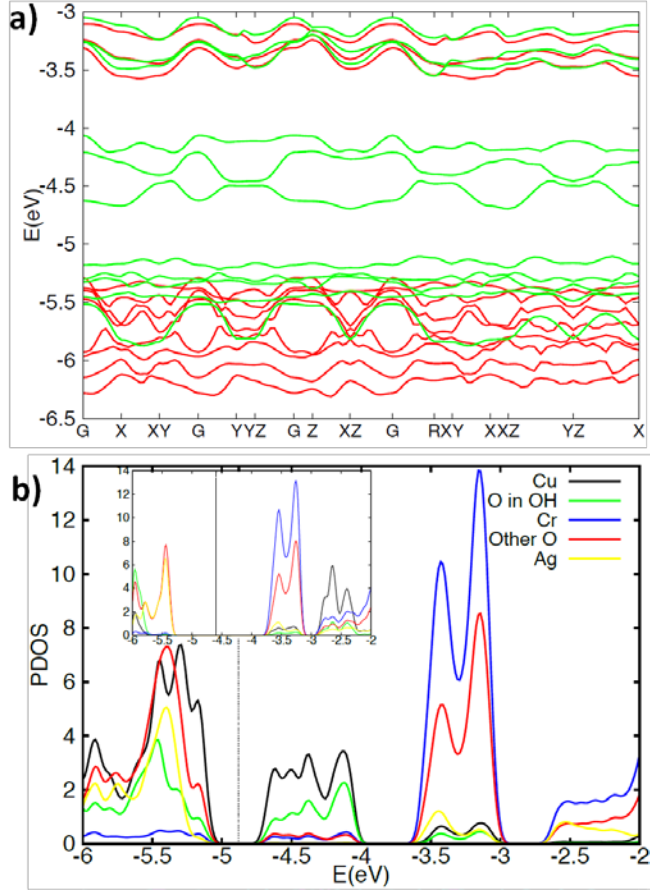


Figure 8. a) Spin-polarized band-structure for the title compound. Red: up (majority) spin, Green: down (minority) spin. b) Partial density of states (PDOS) diagram showing the mainly Cu and O character of the hole bands extending from -4.6 to -4 eV in a). Inset: PDOS for the case of $U = 6$ eV. Note the use of a 0.1 eV Gaussian broadening in the curves. Fermi levels, formally at the center of the gap, are indicated by dotted lines.

Using the energies of the various spin configurations we can determine the three parameters of our model. For example:

$$J_1 = \Delta E(uuu|ddd) / 16 \quad (\text{Equation 2})$$

$$J_2 = (\Delta E(duu) - 4 J_1) / 8 \quad (\text{Equation 3})$$

$$J_3 = (\Delta E(udu) - 6 J_1 - 4 J_2) / 2 \quad (\text{Equation 4})$$

(As a check, the parameters thus determined are consistent with the value of $\Delta E(duu|udd)$). The J values are displayed in Table 3. The largest parameter in absolute value is J_3 , and is negative, implying an antiferromagnetic coupling between Cu2 and Cu3 in the direction perpendicular to b . J_2 is positive, giving ferromagnetic coupling in a number of Cu-Cu links, and J_1 is very small. It is noteworthy that the vanishing J_1 is directly related to the difference in energy between the $uuu|ddd$ and $uuu|uuu$ configurations, implying that there is almost no cost for an alternating spin pattern along the a lattice direction.

In order to investigate the competition between the different J s and their net effect on the magnetic ordering of the compound we performed Monte Carlo simulations with the effective Hamiltonian of Equation 1, considering a two-dimensional array of 40x40 unit cells, each with three sites corresponding to Cu1, Cu2, and Cu3. Appropriate averages were obtained over 80000 lattice sweeps, after proper thermalization. For our purposes of qualitative analysis it is adequate to use a simple Ising model, rather than a Heisenberg one, and to carry out classical rather than quantum MC calculations. We show on Figure 9 the temperature dependence of the averages $\langle s_i s_j \rangle$, which measure the degree of correlation of the spin orientation in sites i and j , classified according to the type of J involved in their interaction, for the case $U = 6$ eV.

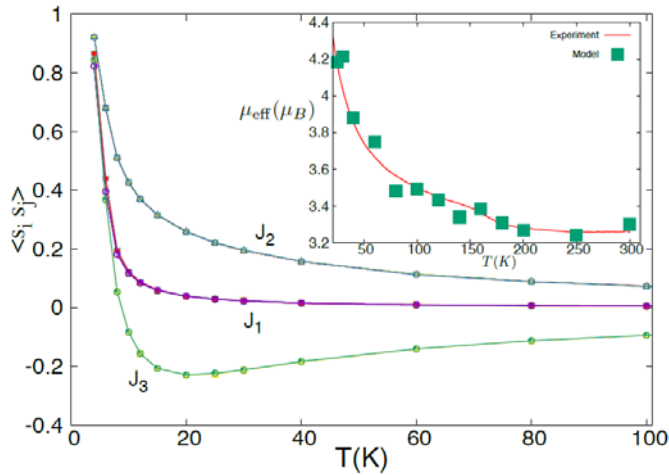


Figure 9. Site correlations as a function of temperature. The curves are a guide to the eye, and are labeled by the J parameter that enters into the corresponding term in Equation 1. Inset: Comparison of the computed μ_{eff} to the experimental data.

Despite its size, J_3 affects only one Cu-Cu link per cell, and is frustrated away at low temperatures by the ferromagnetic interactions, which are smaller but couple all the remaining links in the structure. The correlations become close to unity at very low temperatures, implying that ferromagnetic ordering will eventually be achieved for these parameter values, but the details of the actual ordering depend on the sign of J_1 , which is in practice impossible to compute accurately as it is too close to zero.

Our model can also produce susceptibility data, by means of the fluctuation formula

$$\chi \propto \frac{1}{kT} (\langle M^2 \rangle - \langle M \rangle^2) \quad (\text{Equation 5})$$

where M is the total magnetization of the system. The computed temperature behavior of $\sqrt{sq(\chi T)}$ is plotted in the inset of Figure 9, rescaled to match the high-temperature limit of the experimental μ_{eff} curve in Figure 6(a). The broad features of the enhancement of μ_{eff} are reproduced. The lowest temperatures have been left out of the comparison due to the uncertainty in the sign of J and the use of a classical simulation.

The pattern of J interactions correlates with a structural feature which is relevant for the magnetic behavior: J_2 and J_3 link sites within "stripes" running along the b lattice vector, whereas J_1 links Cu sites at the frontiers of the stripes (see Figure 10). A ferromagnetic J_2 and a frustrated antiferromagnetic (AF) J_3 make these stripes ferromagnetically correlated, and a very small J_1 means that there is either no inter-stripe order or (at very low temperatures) a very weak antiferromagnetic or ferromagnetic stripe arrangement, depending on the actual value of J_1 . On the other hand, it is not clear whether one could consider the stripes as "super-paramagnetic" units, since, as shown in the Supplementary Information (Figure S5), their "ordering temperature" is likely to be below 5 K. In any case we can explain qualitatively the observed ferromagnetic correlations and the fact that the material is experimentally very soft with vanishing remanence and coercivity.

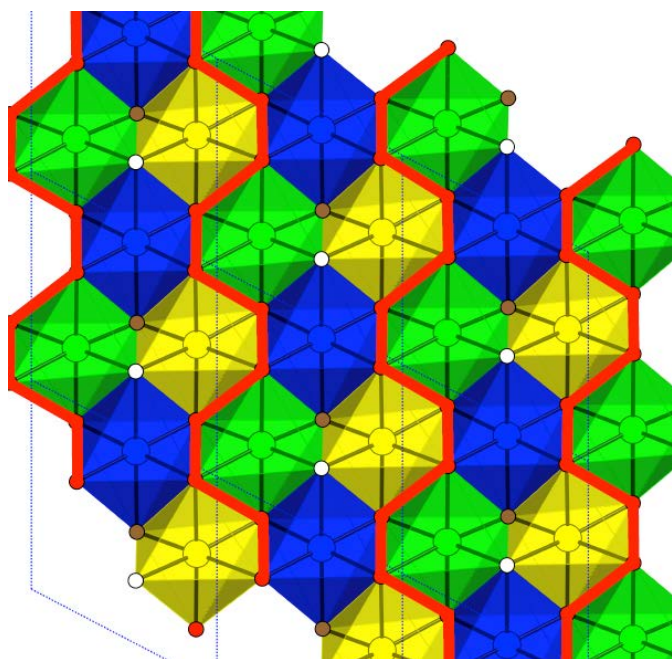


Figure 10. Sketch showing the outline of a ferromagnetically correlated stripe (shown in red). The stripes run parallel to the b lattice direction, and are also parallel to the lines of chromate groups on both sides of the layer (indicated here by the O1A and O1B oxygen sites in brown and white, respectively). Cu Cu₂ Cu₂'

The coupling between different Cu layers is expected to be extremely small, since there are two interposed layers, the Cr-based one (with Cr⁶⁺ formally in a d^0 configuration), and the Ag-based. DFT calculations indeed showed a residual role for Cr in the hole bands, and a negligible one for Ag one. Indeed, DFT calculations, which already showed a residual role for Cr in the hole bands, and a negligible one for Ag, confirm that there is no change in energy when the spin configuration is changed in alternate Cu layers. This situation is different from the case of the reported Ag₂CuMnO₄, where the single Ag layers allow long range antiferromagnetic coupling of the Cu and Mn layers through the large silver d_{10} ions.³¹

In summary, the calculations qualitatively support the experimental results and suggest an interpretation for them, with a simple model for exchange interactions among copper ions in the compound.

4. CONCLUSIONS

A new Ag-Cu-Cr-O mixed oxide has been obtained by hydrothermal oxidizing reactions at low temperature. The new compound, with formula $\text{Ag}_2\text{Cu}_3\text{Cr}_2\text{O}_8(\text{OH})_4$, is red and forms as micron-size pseudo-hexagonal platelets, larger than previously prepared Ag-Cu oxides. We have used direct methods to solve the crystallographic structure of $\text{Ag}_2\text{Cu}_3\text{Cr}_2\text{O}_8(\text{OH})_4$, which crystallizes with a layered ordering containing alternating Ag-O and Cu-O brucite-type layers connected by chromate groups. The structure has been confirmed by XPS and XANES characterization and the electronic structure derived from DFT calculations. $\text{Ag}_2\text{Cu}_3\text{Cr}_2\text{O}_8(\text{OH})_4$ shows in-plane ferromagnetic coupling between copper ions with effective moment increasing rapidly at much higher temperatures than for other reported Cu-based brucitic structures, but there is no evidence of long-range magnetic order. *Ab initio* calculations and Monte Carlo simulations show that the magnetic interactions are two-dimensional in character, and suggest that weakly coupled magnetized stripes are responsible for the non-hysteretic behavior.

Interestingly, $\text{Ag}_2\text{CuMnO}_4$,³¹ another layered Ag-Cu mixed oxide previously reported, also showed ferromagnetic coupling in the same type of 2D arrangement, but in that case it was accompanied by an antiferromagnetic interaction between layers, through silver atoms. In $\text{Ag}_2\text{Cu}_3\text{Cr}_2\text{O}_8(\text{OH})_4$, the existence of two layers (Cr and Ag) between the brucitic Cu layers makes the coupling purely bidimensional, a unique example in the field of silver copper oxides. The bidimensional magnetic coupling is also scarce enough to give additional interest from basic and applied points of view. The structure of this new Ag-Cu-O phase as compared with previous reported silver copper oxides such as $\text{Ag}_2\text{Cu}_2\text{O}_3$, $\text{Ag}_2\text{Cu}_2\text{O}_4$ or $\text{Ag}_2\text{CuMnO}_4$ adds evidence to the conclusion that Ag-Cu layered ordering is favored in heterogeneous oxidizing conditions, while the anion present in the process imposing a coordination is relevant in the final structure. Layered structures result from the soft methods in oxidizing conditions, while high temperature methods seem to favour three-dimensional structures. These empirical correlations offer further insights for the discovery of new members in the sparse family of silver-copper oxides, in which a variety of electronic properties are being found.

ACKNOWLEDGMENTS

The authors would like to acknowledge financing from the Spanish Ministry of Science and of Economy through grants *PB98-0491*, CSIC Ref. 201560E053, MAT2015-65192-R *MAT2011-24363*, *MAT2012-35247*, *FIS2012-37549-C05-05* and *FIS2015-64886-C5-4-P*, as well as the “Severo Ochoa” Program for Centers of Excellence in R&D (SEV-2015-0496), and from Generalitat de Catalunya (2014 SGR 301). We thank Diamond Light Source for provision of beamtime for Cr K-edge XANES experiments and Diego Gianolio for his assistance with the experiments on We thank Enric Canadell, Pablo García-Fernández and Benjamín Martínez for their insightful comments. DMR acknowledges Marie Curie Actions (FP7/2007-2013, Grant Agreement No. 631111). The synchrotron diffraction experiments were performed at MSPD at ALBA Synchrotron with the collaboration of ALBA staff (experiment 2013100638). B18.

REFERENCES

- 1 R. Cava, *Chem. Commun.*, 2005, 5373–5377.
- 2 S. R. Foltyn, L. Civale, J. L. Macmanus-Driscoll, Q. X. Jia, B. Maiorov, H. Wang and M. Maley, *Nat. Mater.*, 2007, 6, 631–642.
- 3 C. N. R. Rao, A. Sundaresan and R. Saha, *J. Phys. Chem. Lett.*, 2012, 3, 2237–2246.
- 4 J. B. Goodenough and Y. Kim, *Chem. Mater.*, 2010, 22, 587–603.
- 5 S. Rühle, A. Y. Anderson, H. N. Barad, B. Kupfer, Y. Bouhadana, E. Rosh-Hodesh and A. Zaban, *J. Phys. Chem. Lett.*, 2012, 3, 3755–3764.
- 6 A. T. Marin, D. Muñoz-Rojas, D. C. Iza, T. Gershon, K. P. Musselman and J. L. MacManus-Driscoll, *Adv. Funct. Mater.*, 2013, 23, 3413–3419.
- 7 Y. S. Lee, J. Heo, S. C. Siah, J. P. Mailoa, R. E. Brandt, S. B. Kim, R. G. Gordon and T. Buonassisi, *Energy Environ. Sci.*, 2013, 6, 2112–2118.
- 8 A. Sawa, *Mater. Today*, 2008, 11, 28–36.
- 9 E. Fortunato, V. Figueiredo, P. Barquinha, E. Elamurugu, R. Barros, G. Gonçalves, S.-H. K. Park, C.-S. Hwang and R. Martins, *Appl. Phys. Lett.*, 2010, 96, 192102.
- 10 S. Nandy, A. N. Banerjee, E. Fortunato and R. Martins, *Rev. Adv. Sci. Eng.*, 2013, 2, 273–304.
- 11 E. Fortunato and R. Martins, *Phys. Status Solidi-Rapid Res. Lett.*, 2011, 5, 336–339.
- 12 K. P. Musselman, A. Wisnet, D. C. Iza, H. C. Hesse, C. Scheu, J. L. MacManus-Driscoll and L. Schmidt-Mende, *Adv. Mater.*, 2010, 22, E254–E258.
- 13 Y. Ievskaya, R. L. Z. Hoye, A. Sadhanala, K. P. Musselman and J. L. MacManus-Driscoll, *Sol. Energy Mater. Sol. Cells*, 2015, 135, 43–48.
- 14 T. Minami, Y. Nishi and T. Miyata, *Appl. Phys. Express*, 2013, 6, 44101.
- 15 S. W. Lee, Y. S. Lee, J. Heo, S. C. Siah, D. Chua, R. E. Brandt, S. B. Kim, J. P. Mailoa, T. Buonassisi and R. G. Gordon, *Adv. Energy Mater.*, 2014, 4, 1301916.
- 16 K. Matsuzaki, K. Nomura, H. Yanagi, T. Kamiya, M. Hirano and H. Hosono, *Appl. Phys. Lett.*, 2008, 93, 202107.
- 17 E. Fortunato, D. Ginley and H. Hosono, *MRS Bull.*, 2007, 32, 242–247.
- 18 H. Kawazoe, M. Yasukawa, H. Hyodo, M. Kurita, H. Yanagi and H. Hosono, *Nature*, 1997, 389, 939–942.
- 19 K. Itohara, S. Shimizu, H. Mukuda, Y. Kitaoka, P. M. Shirage, H. Kito and A. Iyo, *Phys. C*, 2010, 470, S140–S141.

- 20 P. Gómez-Romero, E. M. Tejada-Rosales and M. R. Palacín, *Angew. Chemie Int. Ed.*, 1999, 38, 524–525.
- 21 E. M. Tejada-Rosales, J. Rodríguez-Carvajal, N. Casañ-Pastor, P. Alemany, E. Ruiz, M. Salah El-Fallah, S. Alvarez and P. Gómez-Romero, *Inorg. Chem.*, 2002, 41, 6604–6613.
- 22 G. J. M. Heline and W. E. Van der Linden, *Anal. Chim. Acta*, 1977, 99–110.
- 23 D. Muñoz-Rojas, J. Fraxedas, J. Oró, P. Gómez-Romero and N. Casañ-Pastor, *Cryst. Eng.*, 2002, 5, 459–467.
- 24 D. Muñoz-Rojas, J. Oró, P. Gómez-Romero, J. Fraxedas and N. Casañ-Pastor, *Electrochem. commun.*, 2002, 4, 684–689.
- 25 D. Muñoz-Rojas, G. Subías, J. Fraxedas, P. Gómez-Romero and N. Casañ-Pastor, *J. Phys. Chem. B*, 2005, 109, 6193–6203.
- 26 D. Muñoz-Rojas, J. Fraxedas, P. Gómez-Romero and N. Casañ-Pastor, *J. Solid State Chem.*, 2005, 178, 295–305.
- 27 J. Curda, W. Klein, H. Liu and M. Jansen, *J. Alloys Compd.*, 2002, 338, 99–103.
- 28 D. Muñoz-Rojas, R. Córdoba, A. Fernández-Pacheco, J. M. De Teresa, G. Sauthier, J. Fraxedas, R. I. Walton and N. Casañ-Pastor, *Inorg. Chem.*, 2010, 49, 10977–10983.
- 29 F. Sauvage, D. Muñoz-Rojas, K. R. Poeppelmeier and N. Casañ-Pastor, *J. Solid State Chem.*, 2009, 182, 374–380.
- 30 N. Casañ-Pastor, P. Gómez-Romero, A. Fuertes, J. M. Navarro, M. J. Sanchis and S. Ondoño, *Phys. C*, 1993, 216, 478–490.
- 31 D. Muñoz-Rojas, G. Subías, J. Oró-Solé, J. Fraxedas, B. Martínez, M. Casas-Cabanas, J. Canales-Vázquez, J. Gonzalez-Calbet, E. García-González, R. I. Walton and N. Casañ-Pastor, *J. Solid State Chem.*, 2006, 179, 3883–3892.
- 32 Y. Akizuki, I. Yamada, K. Fujita, H. Akamatsu, T. Irifune and K. Tanaka, *Inorg. Chem.*, 2013, 52, 13824–13826.
- 33 M. Sofin, E. Peters and M. Jansen, *Z. Krist. NCS*, 2003, 218, 379–380.
- 34 Z. Liu, J. Han, K. Guo, X. Zhang and T. Hong, *Chem. Commun.*, 2015, 51, 2597–2600.
- 35 D. Muñoz-Rojas, *Mater. Today*, 2011, 14, 119.
- 36 F. Wang, C. Eylem, K. Nanjundaswamy and N. Iltchev, *Electrochem. Solid-State Lett.*, 2004, 7, A346–A347.
- 37 P. Gómez-Romero, E. Tejada-Rosales, D. Muñoz-Rojas, N. Casañ-Pastor, G. Mestl and H.-J. Wölk, *Patent 20020 309 OEPM*, 2003.

- 38 T. F. T. Cerqueira, S. Lin, M. Amsler, S. Goedecker, S. Botti and M. A. L. Marques, *Chem. Mater.*, 2015, 27, 4562–4573.
- 39 A. J. Dent, G. Cibir, S. Ramos, A. D. Smith, S. M. Scott, L. Varandas, M. R. Pearson, N. A. Krumpa, C. P. Jones and P. E. Robbins, *J. Phys. Conf. Ser.*, 2009, 190, 12039.
- 40 B. Ravel and M. Newville, *J. Synchrotron Radiat.*, 2005, 12, 537–541.
- 41 F. Fauth, I. Peral, C. Popescu and M. Knapp, *Powder Diffr.*, 2013, S2, 360–370.
- 42 P. E. Werner, L. Eriksson and M. Westdahl, *J. Appl. Crystallogr.*, 1985, 18, 367–370.
- 43 O. Vallcorba, J. Rius, C. Frontera, I. Peral and C. Miravittles, *J. Appl. Crystallogr.*, 2012, 45, 844–848.
- 44 J. Rius, *Acta Crystallogr. Sect. A Found. Crystallogr.*, 2011, A67, 63–67.
- 45 I. D. Brown and D. Altermatt, *Acta Crystallogr. Sect. B Struct. Sci.*, 1985, 41, 244–247.
- 46 J. M. Soler, E. Artacho, J. D. Gale, A. Garcia, J. Junquera, P. Ordejon and D. Sanchez-Portal, *J. physics. Condens. Matter*, 2002, 14, 2745–2779.
- 47 E. Anglada, J. M. Soler, J. Junquera and E. Artacho, *Phys. Rev. B*, 2002, 66, 205101.
- 48 J. Moreno and J. M. Soler, *Phys. Rev. B*, 1992, 45, 13891–13898.
- 49 J. P. Perdew, K. Burke and M. Ernzerhof, *Phys. Rev. Lett.*, 1996, 77, 3865–3868.
- 50 S. L. Dudarev, G. A. Botton, S. Y. Savrasov, C. J. Humphreys and A. P. Sutton, *Phys. Rev. B*, 1998, 57, 1505–1509.
- 51 C. M. Ionica-Bousquet, D. Muñoz-Rojas, W. J. Casteel Jr., R. M. Pearlstein, G. G. Kumar, G. P. Pez and M. R. Palacín, *J. Power Sources*, 2011, 196, 1626–1631.
- 52 A. Rabenau and H. Rau, *Philips Tech. Rev.*, 1969, 30, 89–96.
- 53 N. E. Brese and M. O’Keeffe, *Acta Crystallogr. Sect. B-Structural Sci.*, 1991, 47, 192–197.
- 54 F. M. Capece, V. Di Castro, C. Furlani, G. Mattogno, C. Fragale, M. Gargano and M. Rossi, *J. Electron Spectros. Relat. Phenomena*, 1982, 27, 119–128.
- 55 C. L. Bianchi, M. G. Cattania and V. Ragaini, *Surf. Interface Anal.*, 1992, 19, 533–536.
- 56 V. Hayez, A. Franquet, A. Hubin and H. Terryn, *Surf. Interface Anal.*, 2004, 36, 876–879.
- 57 P. Steiner, V. Kinsinger, I. Sander, B. Siegwart, S. Hufner, C. Politis, R. Hoppe and H. Muller, *Zeitschrift fur Phys. B-Condensed Matter*, 1987, 67, 497–502.
- 58 M. C. Biesinger, B. P. Payne, A. P. Grosvenor, L. W. M. Lau, A. R. Gerson and R. S. C. Smart, *Appl. Surf. Sci.*, 2011, 257, 2717–2730.
- 59 F. Farges, *Phys. Chem. Miner.*, 2009, 36, 463–481.
- 60 J. B. Goodenough, *J. Phys. Chem. Solids*, 1958, 6, 287–297.

- 61 J. Kanamori, *Prog. Theor. Phys.*, 1957, 17, 177–196.
- 62 J. Kanamori, *Prog. Theor. Phys.*, 1957, 17, 197–222.
- 63 E. Ruiz, P. Alemany, S. Alvarez and J. Cano, *J. Am. Chem. Soc.*, 1997, 119, 1297–1303.
- 64 N. Casañ-Pastor, J. Bas-Serra, E. Coronado, G. Pourroy and L. C. W. Baker, *J. Am. Chem. Soc.*, 1992, 114, 10380–10383.
- 65 V. Laget, M. Drillon, C. Hornick, P. Rabu, F. Romero, P. Turek and R. Ziessel, *J. Alloys Compd.*, 1997, 262–263, 423–427.
- 66 E. Ruiz, M. Llunell, J. Cano, P. Rabu, M. Drillon and C. Massobrio, *J. Phys. Chem. B*, 2006, 110, 115–118.
- 67 A. V. Koshelev, E. A. Zvereva, D. A. Chareev, O. S. Volkova, A. Vymazalova, F. Laufek, E. V. Kovalchuk, B. Rahaman, T. Saha-Dasgupta and A. N. Vasiliev, *Phys. Chem. Miner.*, 2016, 43, 43–49.
- 68 B. Himmetoglu, R. M. Wentzcovitch and M. Cococcioni, *Phys. Rev. B*, 2011, 84, 115108.